Nanotechnology **18** (2007) 424026 (9pp) doi:10.1088/0957-4484/18/42/424026

Ab initio simulation of magnetic tunnel junctions

Derek Waldron, Lei Liu and Hong Guo

Centre for the Physics of Materials and Department of Physics, McGill University, Montreal, PQ, H3A 2T8, Canada

Received 7 May 2007, in final form 21 June 2007
Published 21 September 2007
Online at stacks.iop.org/Nano/18/424026

Abstract
In this paper, we present the mathematical and implementation details of an *ab initio* method for calculating spin-polarized quantum transport properties of atomic scale spintronic devices under external bias potential. The method is based on carrying out density functional theory (DFT) within the Keldysh non-equilibrium Green's function (NEGF) formalism to calculate the self-consistent spin densities. We apply this method to investigate nonlinear and non-equilibrium spin-polarized transport in a Fe/MgO/Fe trilayer structure as a function of external bias voltage.

1. Introduction

The physics of tunneling magnetoresistance (TMR) and its application to electronic devices has been an area of tremendous experimental and theoretical interest over the last two decades [1–5]. Based on the TMR effect, nanostructured magnetic tunnel junctions (MTJs) are a promising technology for magnetoresistive random access memory (MRAM), magnetic sensors and possibly programmable logic devices [1]. The simplest MTJ consists of two ferromagnetic metal leads sandwiching a very thin insulating barrier layer. The TMR effect [6] in MTJs originates from the quasi-particle electronic structure of the ferromagnetic leads which depends on their magnetization orientation. The tunneling conductance tends to be smallest when the orientations are opposite, leading to a spin valve character [6–10].

An important measure of device merit is the TMR ratio which is defined as $R_{\mathrm{TMR}} = (I_{\mathrm{PC}} - I_{\mathrm{APC}})/I_{\mathrm{APC}}$, where $I_{\mathrm{PC}}, I_{\mathrm{APC}}$ are total tunneling current for parallel configuration (PC) and anti-parallel configuration (APC) of the magnetization moments of the ferromagnetic leads. A larger R_{TMR} gives a more sensitive device which is desirable. Until rather recently, many different MTJs produced a modest R_{TMR} at $\lesssim$70% at room temperature or low temperature, and a major research goal has been the realization of devices with higher R_{TMR}. Following the prediction and elegant physics explanation [11, 12] that Fe/MgO/Fe MTJs may have extremely high R_{TMR}, there has been significant recent advances in the fabrication of MgO-based MTJ with measured room-temperature R_{TMR} of the order of several hundred percent [13–15].

The tremendous success of first principles modeling [11, 12] in helping drive the discovery of new materials for MTJ application illustrates the importance of such *ab initio* techniques to the larger field of spintronics. For instance, in addition to the intense research efforts devoted to studying devices composed of inorganic materials, there have been recent attempts to use organic molecular layers as the tunneling barrier which offer an interesting approach where spin-polarized transport can be tuned by the peculiarities of the organic molecule [16, 17]. In particular, π-conjugated organic semiconductors (OSEs) are a relatively new class of electronic materials that are revolutionizing important technology applications including information display and large-area electronics. The OSEs have weak spin–orbit interaction and large spin coherence giving rise to very long spin diffusion lengths, making them good candidates for spin-polarized electron injection and transport applications. Xiong *et al* reported the injection, transport and detection of spin-polarized carriers using 8-hydroxy-quinoline aluminum (Alq3) molecules as the spacing region of a spin-valve structure, and obtained low-temperature R_{TMR} as large as 40% [16]. Petta *et al* found that spin polarization can be maintained during the tunneling process through an organic monolayer and demonstrated R_{TMR} values of 16% in Ni/octanethiol/Ni MTJs [17].

Spin-polarized quantum transport in nanostructured MTJs has been very sensitive to the chemical and material details of the device. Therefore, to understand these transport features, atomic calculations are often necessary [11, 12] to supplement general physical considerations and arguments [6]. In this regard, several density functional theory (DFT) based first principles methods have been popular in studying coherent spin-polarized tunneling in MTJ. First, a very fruitful approach

is the layer Korringa–Kohn–Rostoker (LKKR) method [18] based on multiple-scattering Green's functions for electronic structure calculations of interfaces [19], where transport is analyzed by calculating Bloch-wave transmission and reflections [20]. The LKKR technique has been used to study spin-dependent tunneling in a number of devices including Fe/ZnSe/Fe and Fe/MgO/Fe tunnel junctions [11, 20, 21]. More recently, Zhang *et al* reported combining LKKR with the non-equilibrium Green's function (NEGF) theory to treat devices under a finite bias [22]. Another very fruitful atomistic technique for analyzing MTJs is the linear muffin-tin orbital (TB-LMTO) electronic structure scheme combined with surface Green's functions [23–25]. More recently, the TB-LMTO has also been combined in some way with NEGF for analyzing finite bias transport situations [26]. So far, both LKKR and LMTO methods for transport rely on the atomic sphere approximation (ASA) whose accuracy requires considerable technical expertise to control.

A different tunneling calculation technique that does not rely on ASA was the embedding potential method due to Inglesfield [27]. Inglesfield derived an energy-dependent surface potential that acts on an embedding interface to include the effect of a bulk crystal. Wortmann *et al* reformulated [28] the Landauer–Büttiker formula to derive an expression for the linear conductance that contains only the embedding potentials of the bulk system and the boundary values of the interface Green's function. Both quantities are available in a standard embedded Green's function calculation and thus it is possible to evaluate conductance for ballistic transport without additional computation. The embedding formalism was implemented within the framework of a full-potential linearized augmented plane-wave (FLAPW) scheme and applied to systems such as Co/Cu/Co tri-layers [28] and tunneling through Fe/MgO/Fe MTJ [29].

Another class of *ab initio* technique for calculating spin-polarized quantum transport is to combine real-space LCAO based DFT with the NEGF where the device leads and the scattering region are treated atomistically on an equal footing. Such a NEGF-DFT technique has been widely used in analyzing nonlinear and non-equilibrium quantum transport in molecular electronics [30–35], and has been adapted to analyze spin-polarized quantum transport recently [36–38]. The basic idea of the NEGF-DFT technique is to use DFT to calculate the Hamiltonian and electronic structure of a device, use NEGF to determine the non-equilibrium quantum statistics that is needed to populate the electronic structure during current flow, and use real-space numerical methods to handle the transport boundary conditions. The NEGF-DFT methods do not rely on ASA. The NEGF-DFT offers a relatively new technique for quantitative analysis of spintronic devices in non-equilibrium from atomic first principles. So far it has been applied to investigate molecular spintronic systems [37, 39, 40], Fe/MgO/Fe MTJ [38], spin transfer torque [41] and magnetoresistance in anti-ferromagnetic tunnel junctions [42].

Using the NEGF-DFT technique, we have calculated the bias dependence of TMR in Fe/MgO/Fe MTJs for which a short account has been published elsewhere [38]. The purpose of this paper is to present some of the technical details of our NEGF-DFT implementation[1] for calculating spin-polarized quantum transport in realistic spintronic devices under finite bias voltage. We formulate the NEGF-DFT formalism in spin-space and introduce k sampling to treat transverse periodic devices. Numerical issues related to computational efficiency, the convergence of k sampling, the hot spots in transmission coefficients with and without bias, etc., will be discussed in detail.

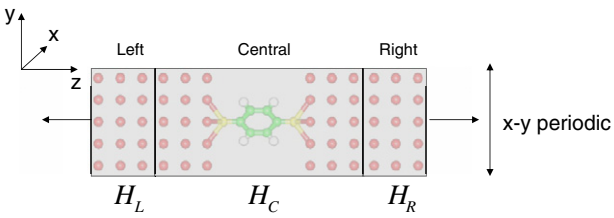

Figure 1. Schematic diagram of an x–y periodic two-probe device. Two semi-infinite ferromagnetic electrodes are contacted via a central scattering region. The electronic structure of the central region is calculated self-consistently where the potential and transport boundary conditions are determined by the left and right ferromagnetic leads which are calculated separately within DFT.

The rest of the paper is organized as follows. In section 2, we briefly outline the theoretical formalism of the NEGF-DFT method for spin-polarized quantum transport calculations. Section 3 presents some implementation details. Section 4 reports the simulation of Fe/MgO/Fe MTJ and the last section is for a short summary.

2. Theoretical formalism

The NEGF-DFT formalism outlined in this paper is a spin-space generalization of the theory described in [30]. We start by considering the general device shown in figure 1 where two semi-infinite ferromagnetic electrodes sandwich a central scattering region. The device is x–y periodic such that the left and right electrodes are fully 3D in a half-plane. It is important to note that, for magnetic systems, 3D leads are necessary in order to correctly describe both the surface and bulk magnetism of the ferromagnets. When applied to molecular spintronic systems involving a single molecule as tunnel barrier [37], the central scattering region must contain enough vacuum so that images of the molecule do not interact. Along the transport direction (z axis), the two ferromagnetic leads extend to reservoirs at $z = \pm\infty$. The central scattering region is chosen sufficiently large in the z direction such that: (i) the potentials outside the central region are taken as equivalent to bulk and (ii) the matrix elements coupling the left and right leads are zero. The electrochemical potentials of the left and right leads, μ_{L} and μ_{R}, are given by the bulk Fermi level of the ferromagnets that can be calculated by DFT at equilibrium, and the applied external bias voltage.

[1] Our NEGF-DFT electronic package is named 'MatDcal', which stands for *Matlab based device calculator* [37]. The code is written in Matlab with a small amount of numerically intensive calculations written in lower level languages. We have developed a parallelization toolbox so that MatDcal can be run in a parallel computer environment. For the calculations presented in this paper, typically 16–32 processors were used in the parallel run.

Because the device is x–y periodic, the eigenstates of the system can be labeled according to their transverse momentum:

$$\Psi^{\mathbf{k}_\parallel}(\mathbf{R}_\parallel + \mathbf{r}) = \mathrm{e}^{\mathrm{i}\mathbf{k}_\parallel\cdot\mathbf{R}_\parallel} \times \mathrm{e}^{\mathrm{i}\mathbf{k}_\parallel\cdot\mathbf{r}}\phi^{\mathbf{k}_\parallel}(\mathbf{r}), \tag{1}$$

where $\mathbf{k}_\parallel$ is a Bloch wavevector, $\mathbf{R}_\parallel = n_x\mathbf{a} + n_y\mathbf{b}$ is a lattice vector and $\phi^{\mathbf{k}_\parallel}$ is the x–y periodic Bloch function. Using the Bloch ansatz, the Schrödinger equation can be written in a matrix form as

$$\tilde{H}^{\mathbf{k}_\parallel}\phi^{\mathbf{k}_\parallel} = E\tilde{S}^{\mathbf{k}_\parallel}\phi^{\mathbf{k}_\parallel}, \tag{2}$$

where $\tilde{H}^{\mathbf{k}_\parallel}$ is the *folded* Hamiltonian defined as

$$\tilde{H}^{\mathbf{k}_\parallel} = \sum_{n_x,n_y} H_{n_x,n_y}\mathrm{e}^{\mathrm{i}\mathbf{k}_\parallel\cdot\mathbf{R}_\parallel}, \tag{3}$$

and overlap matrix $\tilde{S}^{\mathbf{k}_\parallel}$ is defined analogously. In this equation, H_{n_x,n_y} is the Hamiltonian matrix connecting two unit cells separated by $\mathbf{R}_\parallel$. It is important to note that these matrices correspond to the entire device and therefore are infinite in dimension.

At the heart of the NEGF-DFT formalism [30] is the Keldysh Green's functions which are required for the calculation of electron density matrix at non-equilibrium and transport properties of the system. The finite part of the retarded Green's function in $\mathbf{k}_\parallel$ space corresponding to the L–C–R (left, central and right) regions of the device is given by

$$G^{\mathrm{R}}_{\mathbf{k}_\parallel} = \begin{pmatrix} \tilde{H}^{\mathbf{k}_\parallel}_{\mathrm{L}} + \Sigma^{\mathbf{k}_\parallel}_{\mathrm{L}} & \tilde{V}^{\mathbf{k}_\parallel}_{\mathrm{L}} & 0 \\ \tilde{V}^{\mathbf{k}_\parallel,\dagger}_{\mathrm{L}} & \tilde{H}^{\mathbf{k}_\parallel}_{\mathrm{C}} & \tilde{V}^{\mathbf{k}_\parallel}_{\mathrm{R}} \\ 0 & \tilde{V}^{\mathbf{k}_\parallel,\dagger}_{\mathrm{R}} & \tilde{H}^{\mathbf{k}_\parallel}_{\mathrm{R}} + \Sigma^{\mathbf{k}_\parallel}_{\mathrm{R}} \end{pmatrix}^{-1}, \tag{4}$$

where $\tilde{H}^{\mathbf{k}_\parallel}_{\mathrm{L}}$, $\tilde{H}^{\mathbf{k}_\parallel}_{\mathrm{R}}$ and $\tilde{H}^{\mathbf{k}_\parallel}_{\mathrm{C}}$ are the finite sub-matrices of $\tilde{H}^{\mathbf{k}_\parallel}$ corresponding to the L, R and C regions, respectively. $\tilde{V}^{\mathbf{k}_\parallel}_{\mathrm{L}}$ ($\tilde{V}^{\mathbf{k}_\parallel}_{\mathrm{R}}$) are the finite sub-matrices connecting the L(R) and C regions. The coupling of the L and R to the remaining part of the semi-infinite electrodes is fully taken into account by the self-energies, $\Sigma^{\mathbf{k}_\parallel}_{\mathrm{L}}$ and $\Sigma^{\mathbf{k}_\parallel}_{\mathrm{R}}$. The partition of the transport system into L–C–R regions has been well known [43] and equation (4) can be easily proved [44].

To analyze spin-polarized transport, the matrices above have been extended into spin space. Each matrix element in the non-spin formalism [30] becomes a two-by-two matrix which specifies spin-up, spin-down and the connection between the two spin spaces [45]:

$$H_{ij} \to \begin{bmatrix} H_{ij,\uparrow\uparrow} & H_{ij,\uparrow\downarrow} \\ H_{ij,\downarrow\uparrow} & H_{ij,\downarrow\downarrow} \end{bmatrix}. \tag{5}$$

There is no restriction of spin collinearity, hence the left and right leads (and possibly any other part of the system) can have arbitrary relative magnetic orientation. For problems such as spin transfer torque [41], anti-ferromagnet tunnel junction [42] and spin–orbital interaction, the calculation capability of non-colinear spin is important. For the rest of this paper we do not consider non-colinearity; all the formulations below are for colinear systems.

The Hamiltonian of each region is calculated self-consistently within DFT by solving the Kohn–Sham equation [46]:

$$\left[-\frac{\nabla^2}{2} + \int \mathrm{d}\mathbf{r}'\,\frac{\rho(\mathbf{r}')}{|\mathbf{r}-\mathbf{r}'|} + V_{\mathrm{ext}}(\mathbf{r}) + V_{\mathrm{xc}}(\mathbf{r})\right]\psi(\mathbf{r}) = \epsilon_i\psi(\mathbf{r}), \tag{6}$$

where $\rho(\mathbf{r})$ is the total electron density, V_{xc} is the exchange–correlation functional and V_{ext} is any external potential including the pseudopotential that defines the atomic core and the applied bias potential that drives current flow. The spin-dependent exchange–correlation potential is treated at the local spin density approximation (LSDA) level [47, 48], where one distinguishes spin-up and spin-down densities $\rho^\alpha = \rho^\uparrow$ or $\rho^\downarrow$, and the total density is given by $\rho = \rho^\uparrow + \rho^\downarrow$.

As discussed above, when the central scattering region includes enough layers of the ferromagnetic lead atoms, the electronic structure of the left and right regions can be safely considered as that of bulk—which can be calculated with a supercell DFT analysis. In other words, in equation (4) the upper and lower parts of the Hamiltonian (e.g. $\tilde{H}^{\mathbf{k}_\parallel}_{\mathrm{L(R)}} + \Sigma^{\mathbf{k}_\parallel}_{\mathrm{L(R)}}$) corresponding to the left and right ferromagnetic electrodes, are calculated as isolated *bulk* material whose electron density is given by the Kohn–Sham single-particle states:

$$\rho(\mathbf{r}) = \sum_i f(E_i)|\psi_i|^2, \tag{7}$$

where $f(E)$ is a Fermi–Dirac distribution. By using the Fermi–Dirac distribution we have assumed that the left and right ferromagnetic leads are in equilibrium contact with their corresponding reservoirs, as is well established in the Landauer–Büttiker transport formulation [44]. These left and right regions have fully periodic boundary conditions and will exhibit the desired bulk magnetism. The $\mathbf{k}_\parallel$-dependent retarded self-energies of each lead, $\Sigma^{\mathbf{k}_\parallel}_{\mathrm{L}}$, $\Sigma^{\mathbf{k}_\parallel}_{\mathrm{R}}$, are determined using the recursion method of periodic 1D systems [49], however with $H_{\mathrm{L(R)}}$ for 1D replaced by $\tilde{H}^{\mathbf{k}_\parallel}_{\mathrm{L(R)}}$ for 3D leads. In constructing the self-energies and potential matrices for each lead, the reference spin direction is rotated to specify the relative magnetic orientation (for example, PC or APC) of the two ferromagnetic leads.

The remaining parts of the Hamiltonian in equation (4) are for the central region: $\tilde{V}^{\mathbf{k}_\parallel}_{\mathrm{L}}$, $\tilde{V}^{\mathbf{k}_\parallel}_{\mathrm{R}}$ and $\tilde{H}^{\mathbf{k}_\parallel}_{\mathrm{C}}$. They are calculated self-consistently using the *non-equilibrium* electron density matrix [30]. The non-equilibrium density matrix is calculated by integrating over the 2D (in the x–y direction) Brillouin zone (BZ) for contributions of each transverse Bloch state:

$$\rho = \int_{\mathrm{BZ}} \mathrm{d}\mathbf{k}_\parallel \rho_{\mathbf{k}_\parallel}, \tag{8}$$

where the density matrix $\rho_{k_\parallel}$ is constructed using the non-equilibrium Green's function $G^<_{\mathbf{k}_\parallel}$:

$$\rho_{k_\parallel} = -\frac{\mathrm{i}}{2\pi}\int_{-\infty}^{\infty}\mathrm{d}\epsilon G^<_{k_\parallel}(\epsilon). \tag{9}$$

Here $G^<_{\mathbf{k}_\parallel}$ is calculated using the Keldysh equation:

$$G^<_{\mathbf{k}_\parallel} = G^{\mathrm{R}}_{\mathbf{k}_\parallel}\Sigma^<_{\mathbf{k}_\parallel}G^{\mathrm{A}}_{\mathbf{k}_\parallel} \tag{10}$$

where $G^{\mathrm{A}}_{\mathbf{k}_\parallel} = (G^{\mathrm{R}}_{\mathbf{k}_\parallel})^\dagger$ is the advanced Green's function. Within a mean-field type theory such as DFT, the lesser self-energy $\Sigma^<_{\mathbf{k}_\parallel}$ is given by a linear combination of the Fermi–Dirac functions of the two leads [44], $\Sigma^<_{\mathbf{k}_\parallel} = \mathrm{i}\Gamma_{\mathrm{L},\mathbf{k}_\parallel}f_{\mathrm{L}} + \mathrm{i}\Gamma_{\mathrm{R},\mathbf{k}_\parallel}f_{\mathrm{R}}$, where the linewidth functions of left and right leads are related to the retarded self-energies, for instance $\Gamma_{\mathrm{L},\mathbf{k}_\parallel} =$

$\frac{i}{2}[\Sigma_L^{\mathbf{k}_\parallel} - (\Sigma_L^{\mathbf{k}_\parallel})^\dagger]$. It is therefore important to note that the calculation of the density matrix for the device scattering region, equation (9), involves a distribution function that is non-Fermi–Dirac, reflecting the non-equilibrium nature of the transport physics. For further discussions of the non-equilibrium transport physics we refer interested readers to the paper of Wingreen *et al* [50] and the book of Datta [44].

Finally, the spin currents (spin-polarized charge currents) are calculated by integrating the contributions from each transverse Bloch state using the Landauer formula:

$$I_\sigma = \frac{2e^2}{h}\int_{BZ} d\mathbf{k}_\parallel \int d\epsilon [f(\epsilon-\mu_L) - f(\epsilon-\mu_R)] \times T_\sigma(\epsilon, \mathbf{k}_\parallel), \quad (11)$$

where the $\mathbf{k}_\parallel$ resolved transmission coefficient is given by

$$T_\sigma(E, \mathbf{k}_\parallel) = \mathrm{Tr}[\Gamma_{L,\mathbf{k}_\parallel}(E) G^A_{\mathbf{k}_\parallel}(E) \Gamma_{R,\mathbf{k}_\parallel}(E) G^R_{\mathbf{k}_\parallel}(E)], \quad (12)$$

where the trace is taken over the spatial, orbital, or any matrix index. Note that each quantity in the right-hand side is defined in spin space (see equation (5)), we have restored the spin index $\sigma = \uparrow, \downarrow$ in the transmission coefficient and the current. The total charge current is calculated by adding the current of each spin channel, $I = I_\uparrow + I_\downarrow$.

The introduction of x–y periodicity dramatically increases the number of calculation steps compared to a 1D device. First, there are significantly more interacting unit cells in the x–y direction. Even with nearest-cell interaction, the central region of a 3D device interacts with 23 neighboring cells (nine between the central plane and each of the left/right planes, and five in the central plane) compared to only three unique interactions in the 1D device. Second, there is an additional $\mathbf{k}_\parallel$ integration for the calculation of the density matrix and the current. For magnetic tunnel junctions, a huge number of $\mathbf{k}_\parallel$ are necessary to converge the results, as will be discussed in more detail below.

3. Numerical details

In the numerical calculations (see footnote 1), we use an s, p, d linear combination of atomic orbitals (LCAO) basis set [45, 51]:

$$\phi_{lm}(\mathbf{r}) = R_l(r) Y_{lm}(\Omega_r), \quad (13)$$

to expand the electronic wavefunctions and construct the matrix elements of equation (4). The atomic cores are defined by standard norm-conserving nonlocal pseudopotentials [52]. Both the pseudopotentials and basis sets (i.e. $R_l(r)$ in equation (13)) can be generated, for instance using the electronic package SIESTA [45] or similar tools.

Special care must be given to the pseudopotentials and basis sets in order to obtain an accurate description of the band structure near the Fermi level, which is particularly important in studying spin-polarized transport. On the one hand, the calculation of the Green's function in equation (4) requires a reasonable sized basis set so that the matrix on the right-hand side is not prohibitively large to be inverted, while, on the other hand a small basis set does not give accurate results. Therefore a reasonable compromise should be adopted. We also found that pseudopotentials and basis sets that accurately reproduce the electronic structure of the electrode and barrier materials do not necessarily reproduce the electronic structure of the more complicated electrode/barrier interface. Therefore, in our calculations these inputs are carefully constructed to accurately reproduce electronic structures of the bulk materials *and* interfaces obtained by a full potential linear augmented-plane-wave (LAPW) method [53]. The latter comparison for a periodic superlattice of Fe(100)/MgO(100) interface with five layers of each material is shown in figure 3(b). For many systems we have studied, such a good comparison can be achieved by adjusting the LCAO basis sets.

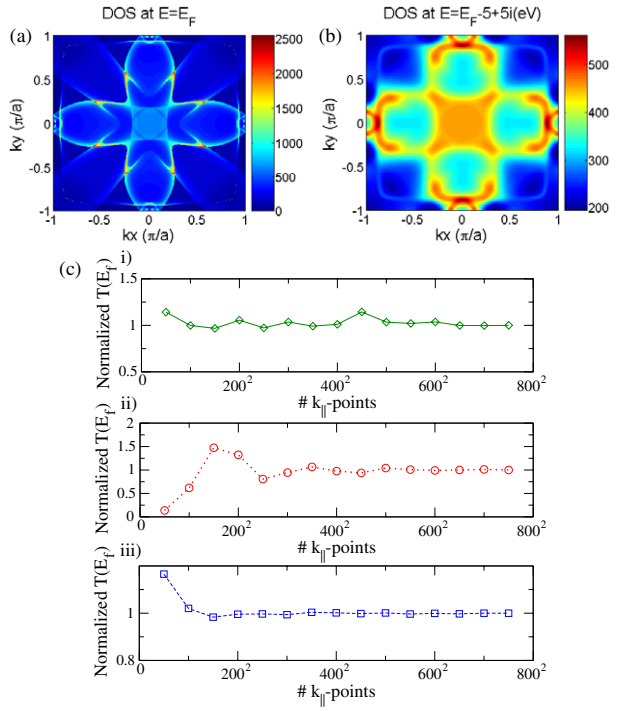

Figure 2. Density of states versus $\mathbf{k}_\parallel$ for a five-layer Fe/MgO/Fe device in PC evaluated (a) on the real energy axis at $E = E_f$ and (b) in the complex plane at $E = E_f - 5 - 5i$ (eV). (c) Convergence of $T(E_f)$ versus number of $\mathbf{k}_\parallel$ points used for integration. (i) Solid line (diamonds): APC; (ii) dotted line (circles): $I_\downarrow$ for PC; (iii) dashed line (squares): $I_\uparrow$ for PC. Note that $T(E_f)$ for each case has been normalized to unity for presentation purposes. Its value is actually very small for APC case.

For MTJ simulations, we found that integration over $\mathbf{k}_\parallel$ must be handled very carefully in order to ensure numerical convergence. We calculate the density matrix using standard complex contour integration for the equilibrium contribution and real-axis integration for the non-equilibrium contribution [30]. The $\mathbf{k}_\parallel$ integration is handled differently for complex energy values on the complex contour versus energy values near the real axis which lies close to the poles of G^R in the lower-half complex energy plane. Figures 2(a) and (b) compare the density of states of a five-layer Fe/MgO/Fe MTJ device in PC as a function of $\mathbf{k}_\parallel$ at $E = E_F$ versus an energy value on the complex contour at $E = E_F - 5 + 5i$ (eV), respectively. This figure clearly shows that a larger imaginary energy component gives rise to a smoother density of states. Because of the smoothness of the DOS for energies on the complex contour (i.e. figure 2(b)), it was found that relatively few $\mathbf{k}_\parallel$ points, for instance $12 \times 12 = 144$ in the full 2D

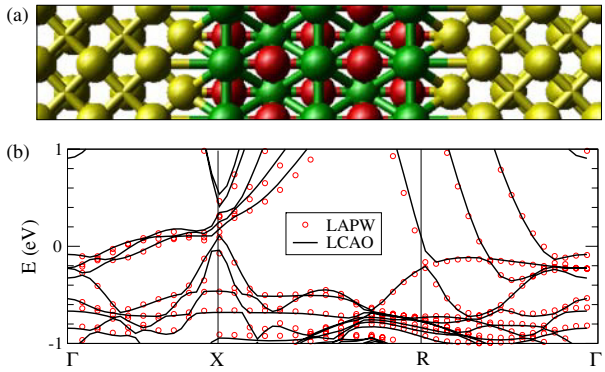

Figure 3. (a) Schematic plot of a two-probe Fe(100)/MgO(100)/Fe(100) device. The system has infinite extent in the (x, y) direction with a lattice constant of 2.82 Å and extends to $\pm\infty$ in the z direction. (b) Band structure of a periodic $\cdots$ Fe/MgO/Fe/MgO$\cdots$ lattice obtained using optimized LCAO pseudopotentials and basis sets compared to that from the full potential LAPW method. A good agreement is found to be necessary in order to carry out the NEGF-DFT analysis for the two-probe Fe/MgO/Fe devices.

Brillouin zone, are sufficient to converge the $\mathbf{k}_\parallel$ integral of the *equilibrium contribution* to the density matrix. On the other hand, it was found that several hundred thousand $\mathbf{k}_\parallel$ points are necessary to converge $\mathbf{k}_\parallel$ integration for quantities evaluated at energy values on the real energy axis, including evaluation of the non-equilibrium contribution to the density matrix and the evaluation of transmission coefficients. Such a necessity of using high-density k-point sampling is consistent with results obtained by other authors [29]. Figure 2(c) plots the relative convergence of the transmission coefficient for the same five-layer Fe/MgO/Fe device for both spin channels in PC and APC as a function of the number of $\mathbf{k}_\parallel$ points used in the integration of equation (9) over the 2D Brillouin zone. These results clearly show that very large numbers of $\mathbf{k}_\parallel$ points are needed for convergence. Fortunately, each $\mathbf{k}_\parallel$ point is calculated separately, thus the calculation can be fully parallelized.

Significant research efforts have been devoted to the development of O(N) electronic structure methods where computational timescales linearly with system size [54, 55]. Most of these techniques are based on direct methods of calculating the density matrix through iterative or minimization schemes in order to avoid an O(N^3) eigenvalue decomposition. For transport, we have developed a reasonably efficient O(N) calculation scheme within the NEGF-DFT framework where the computational timescales linearly with the size of the central region along the z axis by exploiting the block-tridiagonal matrix structure of $H^{\mathbf{k}_\parallel}$ and using the method of inverse by partitioning [57] for the evaluation of equation (4). Suppose that an $N \times N$ matrix A is partitioned into

$$A = \begin{bmatrix} A_{11} & A_{12} \\ A_{21} & A_{22} \end{bmatrix}, \tag{14}$$

where A_{ii} are square matrices although not necessarily of the same dimension. If the inverse of A is partitioned in the same manner,

$$A^{-1} = \begin{bmatrix} \tilde{A}_{11} & \tilde{A}_{12} \\ \tilde{A}_{21} & \tilde{A}_{22} \end{bmatrix}, \tag{15}$$

then $\tilde{A}_{ij}$ which have the same size as A_{ij}, can be found by the following formula [57]:

$$\begin{aligned} \tilde{A}_{11} &= (A_{11} - A_{12}A_{22}^{-1}A_{21})^{-1} \\ \tilde{A}_{12} &= -\tilde{A}_{11}A_{12}A_{22}^{-1} \\ \tilde{A}_{21} &= -A_{22}^{-1}A_{21}\tilde{A}_{11} \\ \tilde{A}_{22} &= A_{22}^{-1} + A_{22}^{-1}A_{21}\tilde{A}_{11}A_{12}A_{22}^{-1}. \end{aligned} \tag{16}$$

The above formulae generalize easily for a block-tridiagonal matrix:

$$B = \begin{bmatrix} B_{11} & B_{12} & 0 & \cdots & 0 & 0 \\ B_{21} & B_{22} & B_{23} & \cdots & 0 & 0 \\ 0 & B_{32} & B_{33} & \cdots & 0 & 0 \\ \vdots & \vdots & \vdots & \ddots & \vdots & \vdots \\ 0 & 0 & 0 & \cdots & B_{n-1,n-1} & B_{n-1,n} \\ 0 & 0 & 0 & \cdots & B_{n,n-1} & B_{nn} \end{bmatrix}, \tag{17}$$

and the corresponding tridiagonal blocks of B^{-1} can be found recursively by [56]

$$\begin{aligned} \tilde{B}_{i,i+1} &= -\tilde{B}_{ii}B_{i,i+1}C_{i+1,i+1} \\ \tilde{B}_{i+1,i} &= -C_{i+1,i+1}B_{i+1,i}\tilde{B}_{ii} \\ \tilde{B}_{i+1,i+1} &= C_{i+1,i+1}(I - B_{i+1,i}\tilde{B}_{i,i+1}) \end{aligned} \tag{18}$$

with $i = 1, 2, \ldots, n-1$ and $\tilde{B}_{11} = C_{11}$, or alternatively by

$$\begin{aligned} \tilde{B}_{i,i+1} &= -D_{ii}B_{i,i+1}\tilde{B}_{i+1,i+1} \\ \tilde{B}_{i+1,i} &= -\tilde{B}_{i+1,i+1}B_{i+1,i}D_{ii} \\ \tilde{B}_{ii} &= D_{ii}(I - B_{i,i+1}\tilde{B}_{i+1,i}) \end{aligned} \tag{19}$$

with $i = n-1, n-2, \ldots, 1$ and $\tilde{B}_{nn} = D_{nn}$, where C_{ii} and D_{ii} are, respectively, defined recursively by

$C_{ii} = [B_{ii} - B_{i,i+1}C_{i+1,i+1}B_{i+1,i}]^{-1}$
with $i = n-1, n-2, \ldots, 1$ and $C_{nn} = B_{nn}^{-1}$, and
$D_{i+1,i+1} = [B_{i+1,i+1} - B_{i+1,i}D_{ii}B_{i,i+1}]^{-1}$
with $i = 1, 2, \ldots, n-1$ and $D_{11} = B_{11}^{-1}$.

In addition, the first and the last column blocks of B^{-1} can recursively be found, respectively, by

$\tilde{B}_{i+1,1} = -C_{i+1,i+1}B_{i+1,i}\tilde{B}_{i,1}$
with $i = 1, 2, \ldots, n-1$ and $\tilde{B}_{11} = C_{11}$, and
$\tilde{B}_{i,n} = -D_{ii}B_{i,i+1}\tilde{B}_{i+1,n}$
with $i = n-1, n-2, \ldots, 1$ and $\tilde{B}_{nn} = D_{nn}$.

Since only the block-tridiagonal matrix elements of $G^{\mathrm{R}}_{\mathbf{k}_\parallel}$ corresponding to overlapping basis functions are required for the equilibrium density matrix, and only additional matrix elements in the first and the last column blocks of $G^{\mathrm{R}}_{\mathbf{k}_\parallel}$ are required for the non-equilibrium density matrix, the above recursive approach can be used for O(N) calculation of these matrix elements. We have implemented this algorithm for calculating density matrix and electric current so that the total calculation timescales as O(N) with respect to the size of the central region along the z axis.

The criteria for convergence during the self-consistent density matrix calculation is $\max(\Delta H) < \delta$, where ΔH is the difference in the Hamiltonian matrix between two consecutive iterations and δ is a pre-specified tolerance. Typical values of δ are 10^{-4} Hartree or less. Broyden's method [58] is used to accelerate convergence, with a typical mixing parameter of $\beta = 0.01$. It was found that convergence during a two-probe calculation typically takes 5–10 times the number of self-consistent iteration steps compared to an equivalent bulk calculation. Therefore, prior to the two-probe calculation a separate bulk calculation of the central cell is performed and the converged spin density is used as the initial density in the two-probe calculation. For devices with non-periodic central cells (i.e. different leads) the separate bulk calculation is performed for a mirror-extended central cell to force periodicity and only half of the converged spin density is used as the initial guess in the final two-probe calculation.

4. Application: MgO magnetic tunnel junction

First-principles calculations [11, 12] have so far played a key role in elucidating the reason behind the observed large TMR in Fe/MgO/Fe MTJs [11–14]. Many first-principles studies have also identified surface roughness and/or oxidization of the Fe/MgO interface as the likely reason for the discrepancy between experimental TMR values and theoretical predictions [25, 38, 59]. However, to date there has been relatively little work on understanding the bias dependence of TMR. Experimental data on MgO-based MTJs show a monotonically decreasing TMR as a function of applied bias voltage [13, 14] reducing to zero on a scale of about 1 V. Early theory [61] on Al_2O_3-based MTJs has attributed small-bias dependence of magnetoresistance to magnon scattering. Previous first-principles calculations of the bias dependence of TMR have predicted a substantial *increase* of TMR versus bias for an Fe/FeO/MgO/Fe device [22], while reference [59] found a roughly constant TMR, a decaying TMR or an entirely negative TMR versus bias for an Fe/MgO/Fe device, depending on the atomic structural details of the interface. More recently, Heiliger *et al* further investigated [60] effects of interface structure on tunneling in MgO devices, and reported different current–voltage behaviors as a function of the interface structure. Given the importance of MgO-based MTJs in near-future spintronics and the accumulated experimental data, further quantitative understanding on quantum transport in Fe/MgO/Fe at finite bias is needed.

Here we present a calculation of the nonlinear and non-equilibrium quantum transport in an Fe/MgO/Fe MTJ using the NEGF-DFT formalism described above. A short account of these results have appeared elsewhere [38]. Our results show that for fully relaxed atomic structure of the Fe/MgO/Fe device, the zero bias equilibrium TMR ratio reaches several thousand percent, consistent with previous theoretical results [11, 62]. Our calculation also shows that this value is drastically reduced to about 1000% if the Fe/MgO interfaces are oxidized by 50% oxygen. We found that the TMR ratio is quenched by bias voltage V_b with a scale of about 1 V, consistent with experimental data. The microscopic details of these transport features can be understood by the behavior of bias-dependent scattering states.

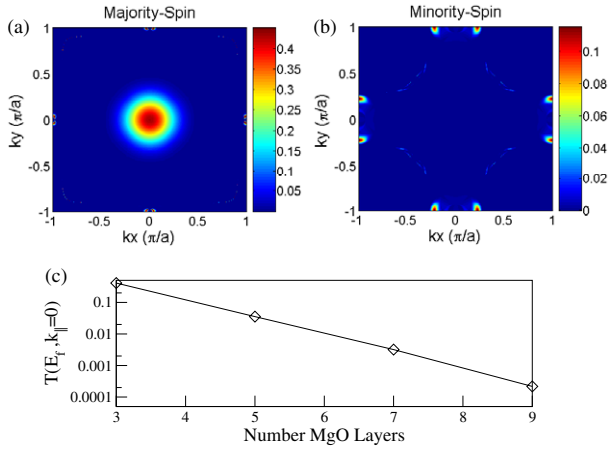

Figure 4. (a), (b) $T(E_F, \mathbf{k}_\parallel)$ for the three-layer PC, majority- and minority-spin, respectively. These figures are to be compared with figure 2(b) of [29]. (c) Semi-log plot of $T(E_f, \mathbf{k}_\parallel = 0)$ versus number of MgO layers.

The MTJ is shown in figure 3(a), where a number of MgO(100) layers are sandwiched by two Fe(100). As discussed above, the MTJ is periodic in the x–y direction and the Fe leads extend to $z = \pm\infty$ (transport direction). The atomic structure was fully relaxed by the LAPW method [53] between three Fe layers on each side of the MgO, with the most remote layer of Fe atoms fixed at crystalline positions during relaxation. The x–y lattice constant a of the interface was fixed to our *calculated* one for bcc Fe, $a = 2.82$ Å. The Fe–O distance was found to be 2.236 Å for a completely relaxed structure, in agreement with previous studies [11]. For the transport calculation, the spin densities were calculated self-consistently for a central region containing eight layers of Fe on either side of the MgO.

Reference [29] reported embedding potential LAPW calculation of equilibrium transmission coefficients for parallel configuration of a three-layer MgO barrier MTJ with Fe leads. To compare, we calculated $T(E_F, \mathbf{k}_\parallel)$ for the majority and minority-spin channels for a three-layer MgO device in PC and the result is plotted in figures 4(a) and (b). Our results are very similar to those reported in [29] (see figure 2(b) of [29]). In particular, the majority-spin transport is dominated by regions around $\mathbf{k}_\parallel = 0$ with circularly symmetric transport pattern, while the minority-spin transport is dominated by $\mathbf{k}_\parallel$ values at the zone boundary. There are small quantitative differences for the minority-spin channel near the zone center: results in [29] show some tiny transmission values near $\mathbf{k}_\parallel \approx 0$, while our calculations show basically zero transmission there. At zone center we obtain a total transmission $T(E, \mathbf{k}_\parallel = 0) = 0.41$, which is in good quantitative agreement to that of [29]. Given that the two methods are totally different in all implementation aspects, i.e. plane waves versus LCAO basis, full potential versus pseudopotential, embedding versus NEGF device partition, as well as differences in the atomic structures, the comparison can be considered as satisfactory. Finally, figure 4(c) shows a semi-log plot of $T(E_F, \mathbf{k}_\parallel)$ in PC for the majority-spin versus the thickness of the MgO barrier, and it shows very good consistency with the physics of tunneling.

Next, we use a five-layer MgO MTJ to show the bias dependence of TMR. Figure 5 plots $T(E_F, \mathbf{k}_\parallel)$ both PC and

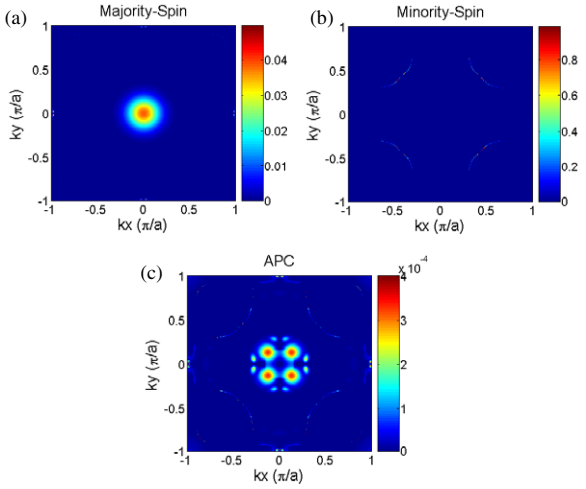

Figure 5. (a), (b) $T(E_F, \mathbf{k}_\parallel)$ for the five-layer PC, majority- and minority-spin, respectively. (c) $T(E_F, \mathbf{k}_\parallel)$ for the five-layer APC.

APC at zero bias. Roughly, $T(E_F, \mathbf{k}_\parallel)$ behaves in a similar way as that of the three-layer MgO device. Namely for PC, the majority-spin transport channel is s-like, i.e. dominated by $\mathbf{k}_\parallel \approx 0$ region; and minority-spin channel has non-zero transmission away from $\mathbf{k}_\parallel = 0$ but the transmission value is much smaller than the majority channel. We find that $T(E_F, \mathbf{k}_\parallel)$ for minority-spin channel exhibits many sharp peaks as a function of $\mathbf{k}_\parallel$ as result of the interface minority-spin state of the Fe/MgO interface, consistent with previous theoretical results [9, 67, 68]. Hence for PC, the total transmission coefficient is dominated by the majority channel. For APC, figure 5(c) shows that $T(E_F, \mathbf{k}_\parallel)$ has a value of the order of 10^{-4}, much smaller than PC transmission. The pattern of $T(E_F, \mathbf{k}_\parallel)$ for APC is also interesting, dominated by four relatively large peaks surrounded by very sharp hot spots. The large difference in transmission values of PC versus APC gives large TMR ratio at zero bias.

Figures 6(a) and (b) plot the calculated current–voltage (I–V) characteristics (solid line) for a five-layer MgO device in PC and APC, respectively[2]. For bias less than 1 V, the total current remains extremely small. At about 1.5 V, the device 'turns on' and current increases rapidly afterward. Such a turn-on voltage is consistent with experimental I–V curve data reported in [63]. The spin currents are shown as the dashed and dotted lines for the up- and down-channels (respectively, majority, minority channel).

We can calculate the TMR ratio R_{TMR} from the I–V curves in APC and PC. At $V_b = 0$ when all currents vanish, we compute R_{TMR} using transmission coefficients. Because R_{TMR} is obtained by dividing a very small number (the APC current), even a small error in APC current makes a large error in R_{TMR}. That is why very large numbers of $\mathbf{k}_\parallel$ points must be sampled for as good a convergence as possible (see lower panels of figure 2). From figure 6(c), for a five-layer MgO

[2] Note that quantitative values in bias-dependent current are somewhat different than the corresponding ones of [38]. In preparing this manuscript, we discovered a small error in the computation of the inner integral (the dϵ integral) of equation (11): the error being the use of an incorrect energy integration limit. This resulted in some quantitative difference in the values but does not lead to a qualitative change of results and conclusions.

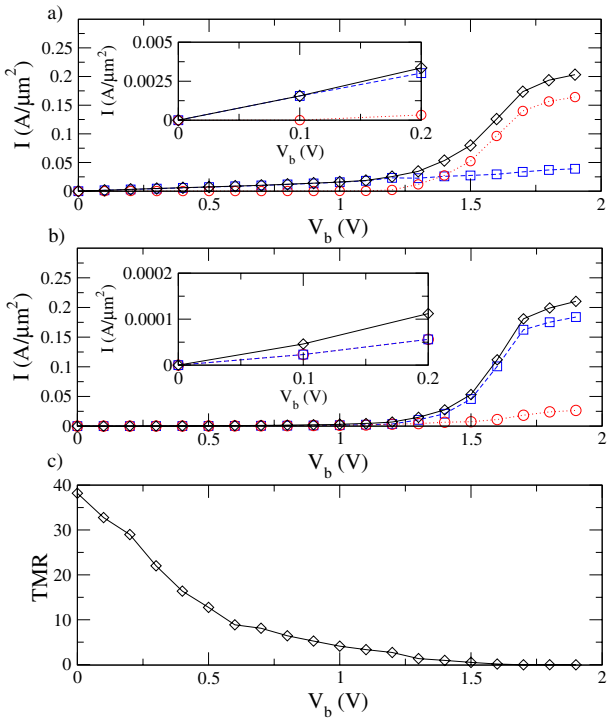

Figure 6. (a), (b) I–V curves for the five-layer PC and APC, respectively. Solid line (diamonds): total current; dashed line (squares): $I_\uparrow$; dotted line (circles): $I_\downarrow$. Inset: I–V curves for small ranges of V_b. (c) TMR versus bias V_b for a five-layer device (diamonds).

device $R_{TMR} \sim 3700\%$ at zero bias and it decays with V_b, essentially vanishing on a scale of about 1 V. For the three-layer MgO device, we found $R_{TMR} \sim 850$ % at zero bias which also decays to zero on a similar bias scale. The decrease in TMR as a function of V_b is in agreement with the experimental data [14, 64].

We also found that drastic changes of zero-bias TMR are obtained when the two Fe/MgO interfaces are oxidized [65]. For two five-layer MgO atomic structures with 100% and 50% oxygen at the interfaces[3], the zero-bias TMR is dropped to ∼169% and ∼1000%, respectively. The reason for this drop is found to be due to a decrease of PC current while the APC current remains at a similar value as that of unoxidized interfaces, consistent with the conclusion of [66].

The voltage dependence of the total current and spin current (figures 6(a) and (b)) can be understood from the behavior of the transmission coefficient T_σ. Figure 7 plots $T_\sigma = T_\sigma(E)$ versus electron energy E at zero bias for PC and APC of the five-layer MgO device. In PC, the majority carrier transmission $T_\uparrow$ (solid line) is smooth and several orders of magnitude larger than $T_\downarrow$ (dashed line) when E is near the Fermi energy of the leads. By analyzing the spin-dependent scattering states [30] of the MTJ, we were able to determine which bands of the Fe leads contribute to the transmission. We found that $T_\uparrow$ is dominated by the Δ_1 band of the Fe leads, in agreement with [11]. Below -1 eV, $T_\uparrow$ becomes extremely small due to the disappearance of the Δ_1 band. The

[3] In our calculations, the atomic structure with oxidization is relaxed using the FLAPW package WIEN2K, see [53].

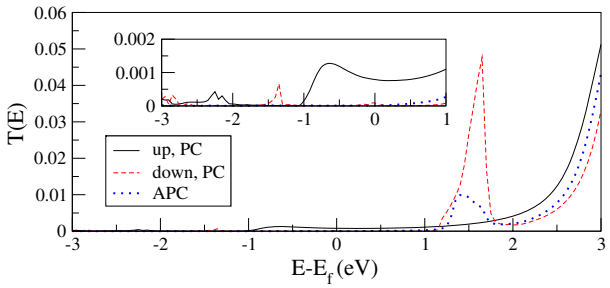

Figure 7. Transmission coefficient T_σ versus energy E for $V_b = 0$, $E = 0$ is the Fermi energy of the leads. Solid line: $T_\uparrow$ for PC set-up; dashed line: $T_\downarrow$ for PC; dotted line: $T_\uparrow = T_\downarrow$ for APC. Inset: the same transmission coefficients at energies between −3 and 1 eV.

$T_\downarrow$, on the other hand, is considerably less smooth because the transmission near the Fermi level is mostly dominated by interface resonance states [67]. In particular, a large peak in $T_\downarrow$ appears above $E = 1$ eV: as E is increased, different Fe bands may participate in transport and this peak is due to such a contribution. This $T_\downarrow$ peak explains the much larger minority-channel current than the majority-channel current in PC at $V_b = 1.5$ V.

For APC, we obtain $T_\uparrow = T_\downarrow$ for all E at zero bias due to the geometrical symmetry of the device. We found that the BZ resolved total transmission, $T(E, \mathbf{k}_\parallel) = T_\uparrow(E, \mathbf{k}_\parallel) + T_\downarrow(E, \mathbf{k}_\parallel)$ for APC shown in figure 8(c) for $V_b = 0$ and figure 8(d) for $V_b = 0.05$ V is dominated by broad and smooth peaks at around $|k_x| = |k_y| = 0.12\pi/a$ (see also figure 5), and there is almost no transmission at $k_x = k_y = 0$. For $V_b = 0$, figure 8(c) also shows that the dominating peaks are surrounded by other much sharper peaks. We found that bias voltage has dramatic effects for APC. The very sharp peaks in figure 8(c), which are due to interface resonances occurring at zero bias, are completely removed by a finite bias of 0.05 V, as shown in figure 8(d). Moreover, the dominating peaks become considerably higher than those in figure 8(c). The origin of the TMR quenching is therefore due to a faster increase of the APC current than the PC current as a function of bias. Thus, our results show that the observed decrease of TMR in Fe/MgO/Fe MTJs as a function of bias voltage can be explained by a simple band-to-band transmission, which is a different mechanism than that proposed to explain TMR quenching in Al_2O_3 MTJs [61].

5. Conclusion

In this paper, we presented the technical details of a relatively new *ab initio* formalism for calculating spin-polarized quantum transport in magnetic tunnel junctions. The technique is based on real-space DFT in combination with the Keldysh non-equilibrium Green's function formalism. We believe the NEGF-DFT method provides a useful alternative and supplements other atomistic techniques for analyzing spin-polarized quantum transport. The main advantage of the NEGF-DFT formalism is its close 'proximity' to modern many-body theory and quantum transport theory which are largely based on Green's functions. As such, new effects and new transport physics can be readily implemented in the NEGF-DFT software tool. From a computational point of view, the NEGF-DFT technique can be implemented into a rather efficient manner so that larger systems can be simulated. By comparing with results obtained from FLAPW, the LCAO basis sets can be tuned to obtain excellent agreement in electronic band structure. For simulating MTJs, it was found that very large numbers of $\mathbf{k}_\parallel$ points are necessary to converge the $\mathbf{k}_\parallel$-dependent quantities such as transmission coefficients and real energy density matrix.

For Fe/MgO/Fe MTJs, our results are consistent with those obtained by LAPW within the embedding potential. The obtained voltage scales for transport features are consistent with experimental data, including the turning-on voltage for currents and the voltage scale for TMR quenching. The quench of TMR by bias voltage is found to be due to a relatively fast increase of channel currents in APC and can be explained by simple band-to-band transmission behavior under bias. Very large TMR at zero bias is obtained which is substantially reduced by oxidization of the Fe/MgO interfaces.

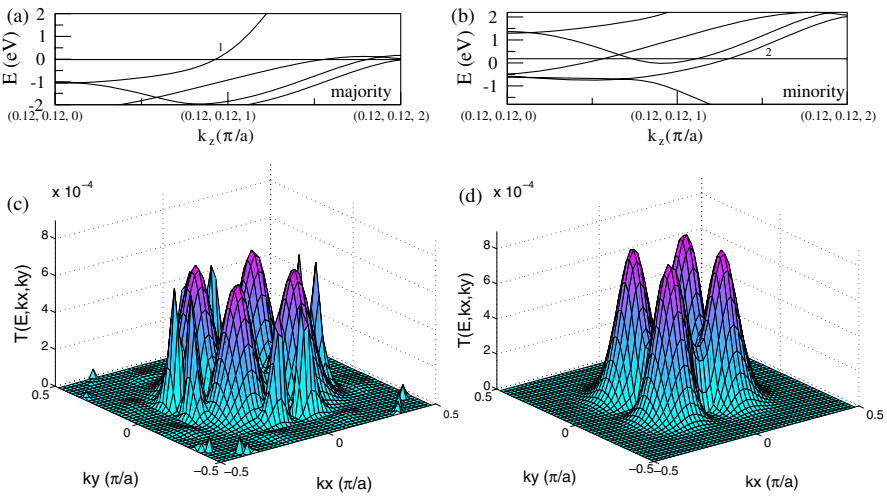

Figure 8. (a), (b) Fe bands at $|k_x| = |k_y| = 0.12\pi$ versus k_z for majority and minority electrons, respectively. (c), (d) Total BZ resolved transmission coefficient at E_f versus k_x, k_y, for five-layer MgO. (c) for $V_b = 0$; (d) for $V_b = 0.05$ V. The dominant peaks are near $|k_x| = |k_y| = 0.12$.

Acknowledgments

We gratefully acknowledge financial support from NSERC of Canada, FRQNT of Quebec, CIAR, Killam Research Fellowship Award (HG). We thank Dr Brian Larade for his contributions in treating the transverse periodic device geometry, Paul Haney for assistance in software developments, Dr Vladimir Timochevskii for creating the pseudopotentials and basis sets used in the calculations presented here, Y B Hu for his participation in earlier stages of the MgO simulation and Professor K Xia for many useful discussions on spin-polarized transport issues.

References

[1] Wolf S A *et al* 2001 *Science* **294** 1488
[2] Wolf S A, Chtchelkanova A Y and Treger D M 2006 *IBM J. Res. Dev.* **50** 1
[3] Zutic I, Fabian J and Das Sarma S 2004 *Rev. Mod. Phys.* **76** 323
[4] Tsymbal E Y *et al* 2003 *J. Phys.: Condens. Matter* **15** R109
[5] Heiliger C *et al* 2006 *Mater. Today* **9** 46
[6] Slonczewski J C 1989 *Phys. Rev.* B **39** 6995
[7] Julliere M 1975 *Phys. Lett.* A **54** 225
[8] Bratkovsky A M 1997 *Phys. Rev.* B **56** 2344
[9] Wang B G, Wang J and Guo H 2001 *J. Phys. Soc. Japan* **70** 2645
[10] Mireles F and Kirczenow G 2002 *Phys. Rev.* B **66** 214415
[11] Butler W H, Zhang X-G and Schulthess T C 2001 *Phys. Rev.* B **63** 054416
[12] Mathon J and Umerski A 2001 *Phys. Rev.* B **63** 220403
[13] Parkin S S P *et al* 2004 *Nat. Mater.* **3** 862
[14] Yuasa S *et al* 2004 *Nat. Mater.* **3** 869
[15] Yuasa S *et al* 2006 *Appl. Phys. Lett.* **89** 042505
[16] Xiong Z H *et al* 2004 *Nature* **427** 821
[17] Petta J R, Slater S K and Ralph D C 2004 *Phys. Rev. Lett.* **93** 136601
[18] Butler W H, Zhang X-G, Nicholson D M C and MacLaren J M 1995 *Phys. Rev.* B **52** 13399
[19] MacLaren J M, Crampin S, Vvedensky D D and Pendry J B 1989 *Phys. Rev.* B **40** 12164
[20] MacLaren J M, Zhang X-G, Butler W H and Wang X 1999 *Phys. Rev.* B **59** 5470
[21] Zhang X-G and Butler W H 2004 *Phys. Rev.* B **70** 172407
[22] Zhang C *et al* 2004 *Phys. Rev.* B **69** 134406
[23] Turek I, Drchal V, Kudrnovsky J, Sob M and Weinberger P 1997 *Electronic Structure of Disordered Alloys, Surfaces and Interfaces* (Boston, MA: Kluwer)
[24] Kudrnovsky J *et al* 2000 *Phys. Rev.* B **62** 15084
[25] Xu P X *et al* 2006 *Phys. Rev.* B **73** 180402
[26] Faleev S V *et al* 2005 *Phys. Rev.* B **71** 195422
[27] Inglesfield J E 1981 *J. Phys. C: Solid State Phys.* **14** 3795
[28] Wortmann D, Ishida H and Blugel S 2002 *Phys. Rev.* B **66** 075113
[29] Wortmann E, Bihlmayer G and Blugel S 2004 *J. Phys.: Condens. Matter* **16** 5819
[30] Taylor J, Guo H and Wang J 2001 *Phys. Rev.* B **63** 245407
[31] Xue Y, Datta S and Ratner M A 2001 *J. Chem. Phys.* **115** 4292
[32] Brandbyge M *et al* 2002 *Phys. Rev.* B **65** 165401
[33] Ke S-H, Baranger H U and Yang W T 2004 *Phys. Rev.* B **70** 085410
[34] Palacios J J *et al* 2002 *Phys. Rev.* B **66** 035332
[35] Lu W C, Vicent M and Bernholc J 2005 *Phys. Rev. Lett.* **95** 206805
[36] Rocha A R and Sanvito S 2004 *Phys. Rev.* B **70** 094406
[37] Waldron D, Haney P, Larade B, MacDonald A and Guo H 2006 *Phys. Rev. Lett.* **96** 166804
[38] Waldron D, Timochevskii V, Hu Y B, Xia K and Guo H 2006 *Phys. Rev. Lett.* **97** 226802
[39] Rocha A R *et al* 2005 *Nat. Mater.* **4** 335
[40] Liu R, Ke S-H, Baranger H and Yang W T 2005 *Nano Lett.* **5** 1959
[41] Haney P M *et al* 2006 *Preprint* cond-mat/0611534
[42] Haney P M *et al* 2007 *Phys. Rev.* B **75** 174428
[43] Caroli C *et al* 1971 *J. Phys. C: Solid State Phys.* **4** 916
[44] Datta S 1995 *Electronic Transport in Mesoscopic Systems* (Cambridge: Cambridge University Press)
[45] Soler J M *et al* 2002 *J. Phys.: Condens. Matter* **14** 2745
[46] Kohn W and Sham L J 1965 *Phys. Rev.* **140** 1133
[47] von Barth U and Hedin L 1972 *Phys. Rev.* B **4** 1629
Gunnarsson O and Lundqvist B I 1976 *Phys. Rev.* B **13** 4274
Rajagopal A K 1978 *J. Phys. C: Solid State Phys.* **11** L943
[48] Perdew J P and Zunger Z 1981 *Phys. Rev.* B **23** 5048
[49] Lopez-Sancho M, Lopez-Sancho L and Rubio J 1984 *J. Phys. F: Met. Phys.* **14** 1205
[50] Wingreen N S, Jauho A-P and Meir Y 1993 *Phys. Rev.* B **48** 8487
[51] Sankey O F and Niklewski D J 1989 *Phys. Rev.* B **40** 3979
[52] Troullier N and Martins J L 1991 *Phys. Rev.* B **43** 1993
[53] Blaha P *et al* 2001 *WIEN2K, An Augmented Plane Wave+Local Orbitals Program for Calculating Crystal Properties* TU Wien, Austria (ISBN 3-9501031-1-2)
[54] Li X-P, Nunes R W and Vanderbilt D 1993 *Phys. Rev.* B **47** 10891
[55] Goedecker S 1999 *Rev. Mod. Phys.* **71** 1850
[56] Wu S Y, Cocks J and Jayanthi C S 1994 *Phys. Rev.* B **49** 7957
[57] Press W H, Flannery B P, Teukolsky S A and Vetterling W T 1992 *Numerical Recipes in C: The Art of Scientific Computing* 2nd edn (Cambridge: Cambridge University Press)
[58] Singh D and Krakauer H 1986 *Phys. Rev.* B **34** 8391
[59] Heiliger C, Zahn P, Yu Yavorsky B and Mertig I 2005 *Phys. Rev.* B **72** 180406
[60] Heiliger C, Zahn P, Yu Yavorsky B and Mertig I 2006 *Phys. Rev.* B **73** 214441
[61] Zhang S, Levy P M, Marley A C and Parkin S S P 1997 *Phys. Rev. Lett.* **79** 3744
[62] Tusche C *et al* 2006 *Phys. Rev. Lett.* **96** 119601
[63] Wulfhekel W *et al* 2001 *Appl. Phys. Lett.* **78** 509
[64] Tiusan C *et al* 2006 *Appl. Phys. Lett.* **88** 062512
[65] Meyerheim H L *et al* 2001 *Phys. Rev. Lett.* **87** 076102
[66] Zhang X-G, Butler W H and Bandyopadhyay A 2003 *Phys. Rev.* B **68** 092402
[67] Wunnicke O *et al* 2002 *Phys. Rev.* B **65** 064425
[68] Belashchenko K D *et al* 2005 *Phys. Rev.* B **72** 140404